2290 *Inorg. Chem.* **2010**, *49*, 2290–2301
DOI: 10.1021/ic902166j

Inorganic Chemistry
Article

Structures and Phase Transitions in $(MoO_2)_2P_2O_7$

Sarah E. Lister,[†] Anne Soleilhavoup,[†] Ray L. Withers,[‡] Paul Hodgkinson,*[,†] and John S. O. Evans*[,†]

[†]*Department of Chemistry, Durham University, Science Laboratories, South Road, Durham, DH1 3LE U.K., and* [‡]*Research School of Chemistry, Australian National University, Canberra, A. C. T, 0200 Australia*

Received November 3, 2009

We report structural investigations into $(MoO_2)_2P_2O_7$ using a combination of X-ray, neutron and electron diffraction, and solid-state NMR supported by first principles quantum chemical calculations. These reveal a series of phase transitions on cooling at temperatures of 377 and 325 K. The high temperature γ-phase has connectivity consistent with that proposed by Kierkegaard at room temperature (but with improved bond length distribution), and contains 13 unique atoms in space group *Pnma* with lattice parameters $a = 12.6577(1)$ Å, $b = 6.3095(1)$ Å, $c = 10.4161(1)$ Å, and volume 831.87(1) Å^3 from synchrotron data at 423 K. The low temperature α-structure was indexed from electron diffraction data and contains 60 unique atoms in space group $P2_1/c$ with cell parameters $a = 17.8161(3)$ Å, $b = 10.3672(1)$ Å, $c = 17.8089(3)$ Å, $\beta = 90.2009(2)°$, and volume 3289.34(7) Å^3 at 250 K. First principles calculations of ^{31}P chemical shift and *J* couplings were used to establish correlation between local structure and observed NMR parameters, and 1D and 2D ^{31}P solid-state NMR used to validate the proposed crystal structures. The intermediate β-phase is believed to adopt an incommensurately modulated structure; ^{31}P NMR suggests a smooth structural evolution in this region.

Introduction

Framework inorganic compounds have a large number of potentially exploitable properties. Zeolites and aluminophosphates find a range of applications from ion exchange and catalysis to use as molecular sieves in applications from water purification and detergents to the petroleum industry.[1] Phosphate materials have been extensively studied as Li intercalation hosts for batteries.[2−4] We have an ongoing interest in framework materials that display interesting properties including negative thermal expansion and complex phase transitions.[5]

Understanding the properties of framework materials requires a detailed knowledge of their structure. However, for many framework materials this is hampered by the occurrence of phase transitions on cooling which can lead to significant complexity at low temperature. For example, in the case of ZrP_2O_7, electron diffraction provided evidence for a $3\times 3\times 3$ superstructure relative to the expected simple cubic unit cell,[6] ^{31}P solid state NMR led to the assignment of space group *Pbca*,[7] and finally a combination of simulated annealing and Rietveld refinement simultaneously on powder X-ray and neutron diffraction data led to the structure solution of the phase,[8] in complete agreement with the solution obtained from a single crystal refinement published simultaneously by a different group.[9]

We have recently investigated the chemistry of materials containing Mo octahedra corner-linked to phosphate tetrahedra. This has led to the discovery of remarkable structural complexity in $Mo_2P_4O_{15}$.[10] Here we discuss structures of the α-, β-, and γ- phases of $(MoO_2)_2P_2O_7$, which is the ultimate phase formed on thermal decomposition of $MoO_2\cdot H_2O\cdot PO_3OH$ at 923 K.[11,12]

The structure of $(MoO_2)_2P_2O_7$ was first described by Kierkegaard[12] in space group *Pnma*, Figure 1, and is referred to hereafter as the subcell model. It was described as containing two unique octahedral Mo sites and two unique tetrahedral P sites. Every MoO_6 octahedron shares two Mo−O vertices with other MoO_6 octahedra, forming zigzag chains in the *ac* plane, and shares three of the four remaining vertices with oxygens of PO_4 tetrahedra. The PO_4 tetrahedra link up to form P_2O_7 groups; these groups are in an eclipsed

*To whom correspondence should be addressed. E-mail: paul.hodgkinson@durham.ac.uk (P.H.), john.evans@durham.ac.uk (J.S.O.E.).

(1) Wright, P. A. *Microporous Framework Solids*; RSC: Cambridge, 2008.
(2) Padhi, A. K.; Nanjundaswamy, K. S.; Goodenough, J. B. *J. Electrochem. Soc.* **1997**, *144*, 1188–1194.
(3) Tarascon, J. M.; Armand, M. *Nature* **2001**, *414*, 359–367.
(4) Armand, M.; Tarascon, J. M. *Nature* **2008**, *451*, 652–657.
(5) Evans, J. S. O. *J. Chem. Soc., Dalton Trans.* **1999**, *19*, 3317–3326.
(6) Withers, R. L.; Tabira, Y.; Evans, J. S. O.; King, I. J.; Sleight, A. W. *J. Solid State Chem.* **2001**, *157*, 186–192.
(7) King, I. J.; Fayon, F.; Massiot, D.; Harris, R. K.; Evans, J. S. O. *Chem. Commun.* **2001**, *18*, 1766–1767.
(8) Stinton, G. W.; Hampson, M. R.; Evans, J. S. O. *Inorg. Chem.* **2006**, *45*, 4352–4358.
(9) Birkedal, H.; Krogh Andersen, A. M.; Arakcheeva, A.; Chapuis, G.; Norby, P.; Pattison, P. *Inorg. Chem.* **2006**, *45*, 4346–4351.
(10) Lister, S. E.; Evans, I. R.; Evans, J. S. O. *Inorg. Chem.* **2009**, *48*, 9271–9281.
(11) Schulz, I. *Z. Anorg. Allg. Chem.* **1955**, *281*, 99–112.
(12) Kierkegaard, P. *Ark. Kemi* **1962**, *19*, 1–14.

 Published on Web 02/04/2010

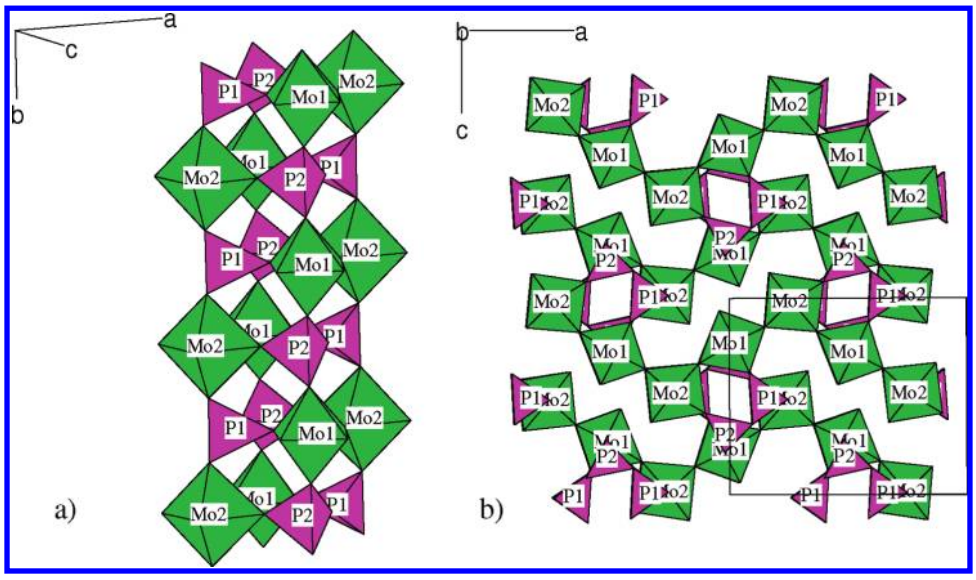

Figure 1. Structural connectivity in $(MoO_2)_2P_2O_7$. (a) Eclipsed P_2O_7 groups link to three different chains of MoO_6 octahedra. (b) Connectivity in the *ac* plane of the structure showing the corner-sharing MoO_6 zigzag chains.

conformation, with all six vertices linking to MoO_6 octahedra. Calculated bond lengths, bond valences, and selected bond angles from the published model are included in Table 1. The reported bond lengths for this crystal structure are considerably distorted relative to similar materials, and bond valence sums are far from ideal.

In fact Kierkegaard described his model as being idealized, as "some of the light atoms should be slightly displaced to give an explanation of very weak zones, indicating a *b* axis being four times that of the sublattice cell."[12] These findings led us to examine the structure of $(MoO_2)_2P_2O_7$ more closely. We have investigated the structure of this material using a combination of X-ray and neutron diffraction and the complementary methods of ^{31}P solid-state NMR, electron diffraction, and theoretical calculations. The experimental NMR results, aided by density functional theory (DFT) calculations, provide particularly useful insights into local structure, and give strong independent confirmation of conclusions drawn from powder diffraction data.

Experimental Section

A typical synthesis of $(MoO_2)_2P_2O_7$ involved dehydration of the precursor material, $MoO_2 \cdot H_2O \cdot PO_3OH$, whose synthesis is described elsewhere.[13] A 2.247 g portion of $MoO_2 \cdot H_2O \cdot PO_3OH$ (9.29 mmol) was heated in an alumina crucible at 5 K/min to 923 K, held at that temperature for 48 h, then cooled in the furnace to room temperature. The synthesis produced 1.633 g of the title material in 82% yield (PDF 74-1380).[14]

Powder diffraction data were recorded on samples of $(MoO_2)_2P_2O_7$ using both laboratory instruments and central facilities. Laboratory X-ray data were collected from 18 to 753 K on a Bruker d8 diffractometer using Cu Kα_1 radiation using an Anton Parr HTK1200 heating stage and an Oxford Cryosystems pHeniX cryostat. Synchrotron X-ray data were collected at temperatures of 250/338/423 K at station ID31 at the ESRF with a wavelength of 0.35285(8) Å and constant wave neutron data at BT-1 at the NCNR using a wavelength of 1.5403(2) Å. TOF neutron data were recorded on the high-resolution powder diffractometer (HRPD) at the ISIS neutron source of the Rutherford Appleton Laboratory, U.K. Data were collected at 250 K over the time-of-flight range 30 to 130 ms (d = 0.62−2.7 Å) for 200 μA h. All Rietveld refinements were performed using the Topas Academic software suite controlled by local routines.[15] Full details of the data acquisitions and protocols for all refinements undertaken are given in the Supporting Information

^{31}P NMR spectra were recorded on a 500 MHz Varian InfinityPlus spectrometer at a frequency of 202.28 MHz. The sample was packed in 5 mm (spin−echo and DQ/SQ dipolar correlation experiments) or 4 mm (all other experiments) zirconia rotors and spun at magic-angle spinning (MAS) rates of between 5 and 15 kHz. ^{31}P chemical shifts were referenced to the signal from $H_3{}^{31}PO_4$ (80% aqueous solution) at 0 ppm. Temperatures were actively controlled to within 1 K, although actual sample temperatures are higher because of frictional heating. Correction factors of up to 24 K were determined from calibration experiments using the temperature dependence of the ^{207}Pb resonance of $PbNO_3$.[16,17]

Spin−lattice (T_1) relaxation times for this sample were relatively long; values between 190 and 330 s for the different sites were determined using saturation recovery experiments. One-dimensional (1D) spectra were obtained using recycle delays of 1024 s to ensure full relaxation and good quantitativity. Two-dimensional (2D) spectra invariably employed pre-saturation, using a train of 100 saturation pulses separated by 1 ms, followed by a recovery period of 133.3 s, to obtain a 2D spectrum in a reasonable experiment time (typically 20 h).

^2J spin−spin couplings were determined from spin echo measurements, using 14 spin echo times (2τ) over the range 4 to 192 ms. The ^{31}P signal intensities, I, were fitted to:

$$I(2\tau) = I(0)\cos(2\pi J\tau)\exp\left(\frac{-2\tau}{T_2'}\right)$$

(13) Kierkegaard, P. *Acta Chem. Scand.* **1958**, *12*, 1701–1714.
(14) Powder Diffraction File; International Centre for Diffraction Data: Newton Square, PA, 1998.
(15) Coelho, A. A. *TOPAS Academic: General Profile and Structure Analysis Software for Powder Diffraction Data*; Bruker AXS: Karlsruhe, Germany, 2004.
(16) Bielecki, A.; Burum, D. P. *J. Magn. Reson. A* **1995**, *116*, 215–220.
(17) van Gorkom, L. C. M.; Hook, J. M.; Logan, M. B.; Hanna, J. V.; Wasylishen, R. E. *Magn. Reson. Chem.* **1995**, *33*, 791–795.

where T_2' is the time constant for decay under a spin echo. The decays fitted well to a single oscillation, that is, longer range couplings were unresolved and absorbed into the signal decay.

2D double quantum/single quantum (DQ/SQ) correlation experiments have been widely used to complement diffraction studies on related framework materials based on pyrophosphate units.[7,18−21] Through-bond DQ/SQ experiments exploiting the P−O−P ^2J couplings were obtained using the refocused INADEQUATE experiment[7,22] at a magic angle spinning (MAS) rate of 15 kHz, using 32 increments in the indirect dimension and 8 transients per increment. Rotation-synchronized periods of 14.6 ms were used for excitation and reconversion of the double quantum coherences under the effect of the ^2J couplings. Dipolar DQ/SQ correlation experiments, exploiting the ^{31}P,^{31}P dipolar couplings, were obtained using the POST-C7 sequence[23] to recouple the dipolar interactions under magic-angle spinning (here at a rate of 8 kHz, with a ^{31}P nutation frequency of 56 kHz during the recoupling). The recoupling period was varied between 0.143 and 1.00 ms to observe the build up of correlations through successively longer range couplings. Spectra were processed using a 40 Hz Gaussian line broadening in both dimensions. This improves the spectral appearance without distorting correlation information, which can be obscured if the 2D lineshapes have significant Lorentzian character.[24]

DFT calculations were performed on $P_2O_7^{4-}$ groups as a function of P−O−P bond angle for both eclipsed and staggered configurations. Model geometries of the $P_2O_7^{4-}$ anions were constructed by fixing the terminal P−O bonds to 1.500 Å and the bridging P−O bonds to 1.583 Å.[25] The O−P−O angles *within* the PO_3 groups were fixed at 112°, and other external O−P−O angles were fixed at 107°. $^2J_{PP}$ coupling constants were computed for P−O−P angles between 100° and 180° at the B3LYP/6-31G*[26−29] level of theory using the Gaussian 03 package[30] for staggered and eclipsed geometries viewed along the P−P vector.

DFT calculations using the CASTEP code[31] were performed to calculate ^{31}P shielding tensors for the different model structures. For the plane wave basis, a cutoff energy of 1200 eV was used, and a *k*-point spacing density of 0.05 Å^{-1} was specified, giving $2 \times 4 \times 2$ and $2 \times 2 \times 2$ sampling grids in the Brillouin zone for the high and low temperature phases, respectively.

Samples for electron microscopy were prepared by crushing and dispersing onto holey-carbon coated molybdenum grids, which were subsequently examined in a Philips EM 430 Transmission Electron Microscope (TEM) operating at ambient temperature and 300 kV. The experimental set up used for SHG tests is described in ref 32.

Results

Thermal Expansion of $(MoO_2)_2P_2O_7$. The temperature dependence of unit-cell parameters *a*, *b*, *c*, and *V* of $(MoO_2)_2P_2O_7$ from 18 to 753 K are shown in Figure 2. Each lattice parameter shows positive thermal expansion over the entire temperature range studied. There is a sharp discontinuity in the *c* parameter at 325 K indicating a phase transition with an overall volume change of $\Delta V \sim +0.3\%$. An approximately 10 K hysteresis in the transition temperature was found on cooling. A second more gradual change in cell parameter at 377 K is visible on close inspection of Figure 2, which is marked by an arrow on the inset to Figure 2c. These transitions are clearer in the variable temperature synchrotron data, insets to Figure 2. Percentage changes in *a*, *b*, and *c* over the whole temperature range of +1.94, +0.05, and +0.61% are observed. For later discussion we will refer to the three phases observed on warming as α-, β-, and γ- $(MoO_2)_2P_2O_7$. Using the Pearson system of nomenclature[33] the α- and γ-materials are the $(MoO_2)_2P_2O_7$ (*mP*240), and (*oP*60) phases, respectively.

High quality data sets (Figure 3) revealed the presence of very weak superstructure peaks present below the 325 K phase transition; these peaks disappear on heating and reappear on cooling. The strongest of these peaks has 0.25% of the intensity of the most intense peak in the pattern. Pawley fitting of the subcell model to the data recorded at 303 and 423 K is shown in Figure 3, and highlights the superstructure peaks. We note that the superstructure peaks are also weak in neutron diffraction patterns, suggesting that changes in both metal and oxygen positions at the phase transition are small.

Variable Temperature ^{31}P Solid-State NMR Results. Only very minor intensity changes are observed in the powder diffraction data over the temperature range 18 to 753 K suggesting a subtle structural change to which diffraction is relatively insensitive. In contrast, ^{31}P NMR spectra show much more marked changes as a function of temperature, as shown in Figure 4.

The NMR spectrum of the high temperature phase contains two signals at −23.7 ppm and −28.5 ppm. Fitting of the complete spectrum (i.e., including spinning sidebands) shows the relative intensities to be equal within the fitting error (< 1%); the slight asymmetry of the centerband intensities is due to a noticeable difference in the chemical shift anisotropies of the two sites. The spectrum at 277 K is significantly more complex, and can be described in terms of a pair of strong signals at −21.2 ppm (a) and −28.8 ppm (e), and a pair of smaller peaks at −23.9 (c) and −27.0 (d) ppm. The signal at −21.2 ppm has a prominent shoulder (b), Figure 5. Fitting of the full spectrum gave relative intensities of 1.9:1.1:1.0:1.0:3.1 for the five resolved features, which

(18) Hartmann, P.; Jana, C.; Vogel, J.; Jager, C. *Chem. Phys. Lett*. **1996**, *258*, 107–112.
(19) Fayon, F.; King, I. J.; Harris, R. K.; Gover, R. K. B.; Evans, J. S. O.; Massiot, D. *Chem. Mater*. **2003**, *15*, 2234–2239.
(20) Fayon, F.; Massiot, D.; Levitt, M. H.; Titman, J. J.; Gregory, D. H.; Duma, L.; Emsley, L.; Brown, S. P. *J. Chem. Phys*. **2005**, *122*, 194313.
(21) Fayon, F.; Le Saout, G.; Emsley, L.; Massiot, D. *Chem. Commun*. **2002**, *16*, 1702–1703.
(22) Lesage, A.; Bardet, M.; Emsley, L. *J. Am. Chem. Soc*. **1999**, *121*, 10987–10993.
(23) Hohwy, M.; Jakobsen, H. J.; Eden, M.; Levitt, M. H.; Nielsen, N. C. *J. Chem. Phys*. **1998**, *108*, 2686–2694.
(24) Robbins, A. J.; Ng, W. T. K.; Jochym, D.; Keal, T. W.; Clark, S. J.; Tozer, D. J.; Hodgkinson, P. *Phys. Chem. Chem. Phys*. **2007**, *9*, 2389–2396.
(25) Lister, S. E.; Evans, I. R.; Howard, J. A. K.; Coelho, A. A.; Evans, J. S. O. *Chem. Commun*. **2004**, *22*, 2540–2541.
(26) Becke, A. D. *J. Chem. Phys*. **1993**, *98*, 1372–1377.
(27) Lee, C. T.; Yang, W. T.; Parr, R. G. *Phys. Rev. B* **1988**, *37*, 785–789.
(28) Petersson, G. A.; Bennett, A.; Tensfeldt, T. G.; Allaham, M. A.; Shirley, W. A.; Mantzaris, J. *J. Chem. Phys*. **1988**, *89*, 2193–2218.
(29) Petersson, G. A.; Allaham, M. A. *J. Chem. Phys*. **1991**, *94*, 6081–6090.
(30) Frisch, M. J. et al. *Gaussian 03*; Gaussian,Inc.: Wallingford, CT, 2004.
(31) Clark, S. J.; Segall, M. D.; Pickard, C. J.; Hasnip, P. J.; Probert, M. J.; Refson, K.; Payne, M. C. *Z. Kristallogr*. **2005**, *220*, 567–570.
(32) Ok, K. M.; Chi, E. O.; Halasyamani, P. S. *Chem. Soc. Rev*. **2006**, *35*, 710–717.
(33) Pearson, W. B. A *Handbook of Lattice Spacings and Structures of Metals and Alloys*; Pergamon Press: Oxford, 1967; Vol. *2*.

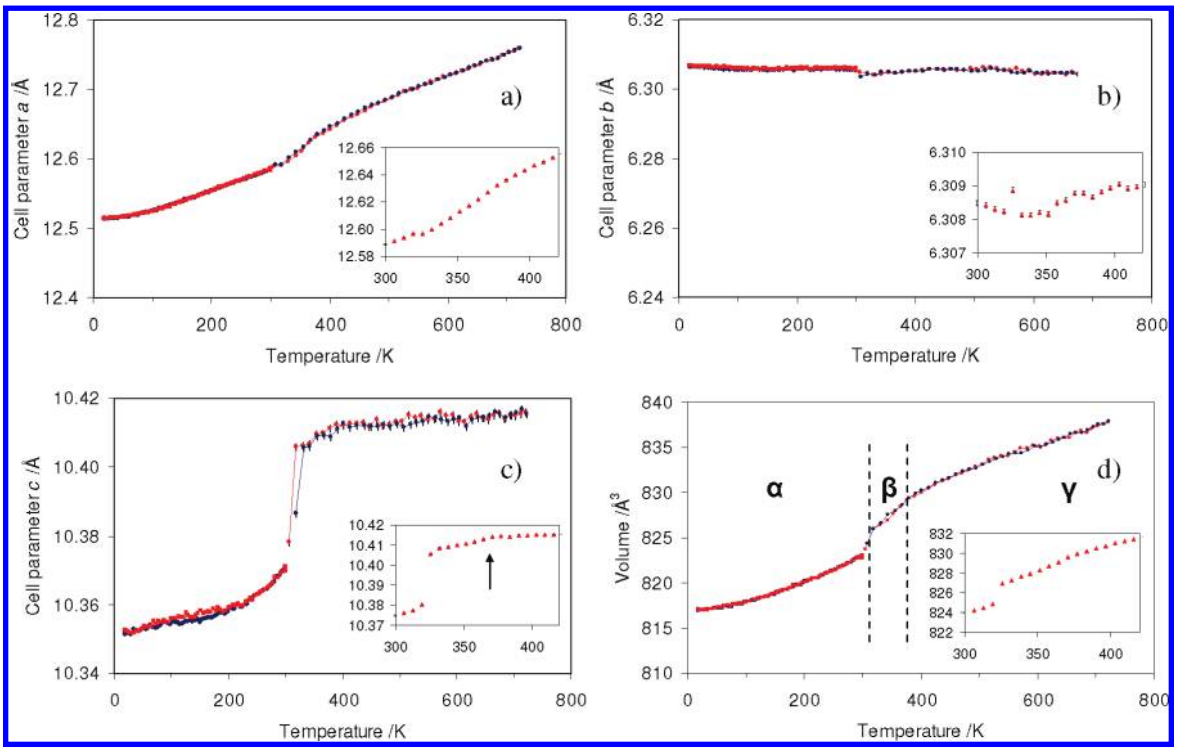

Figure 2. Temperature evolution of the $(MoO_2)_2P_2O_7$ subcell unit-cell parameters *a*, *b*, *c* and volume from laboratory powder data. Insets: refined parameters from synchrotron data over the temperature range 300−420 K.

is in excellent agreement with a 2:1:1:1:3 multiplicity ratio. Further details of the fitting results are given in the Supporting Information (Tables S1 and S2 and Figures S1 and S2).

As the temperature is increased, there is some systematic drift of the peaks (particularly noticeable for the b and c peaks) before a major broadening occurs over the range 340−360 K (the range over which the β-phase is observed in powder diffraction experiments. This broad spectrum then smoothly resolves into the simple spectrum of the high temperature form as the temperature is further raised. The intermediate spectra strongly suggest a structure containing a range of phosphorus environments; the form of the spectra is much more consistent with a static distribution of environments than a broadening because of dynamic exchange.

High Temperature Structure of γ-$(MoO_2)_2P_2O_7$. 1D ^{31}P NMR experimental results are consistent with a single P_2O_7 group being present at high temperature. This was confirmed by the 2D and spin−echo experiments described later and is entirely consistent with the room temperature subcell model originally proposed by Kierkegaard.[12] However, the bond lengths and angles in the published structure (Table 1) are far from ideal for molybdenum phosphate species.

Refinements of the subcell structure were therefore carried out against high temperature synchrotron (423 K) and neutron (500 K) data. These led to a much improved model showing bond length distortions within the Mo octahedra as expected, as discussed by Costentin.[34−36] They state that the Mo atom is displaced out of the basal plane toward one of the oxygens, forming a short (∼1.65 Å) molybdenyl bond. The bond "opposite" the short bond is longer, with lengths varying from ∼2.15 Å in a Mo−O−P arrangement, 2.40 Å in a Mo−O−Mo double octahedral arrangement, and between 2.7 and 2.9 Å for chains of molybdenum octahedra.

The Rietveld fits of the synchrotron and neutron data are given in Figure 6. They are shown on a $\sqrt{I}$ scale to emphasize the weak features in the data. Revised bond lengths are given in Table 1 alongside those calculated from the published model prior to refinement of atomic coordinates. Selected refinement details are given in Table 2. Refinement of the atomic coordinates leads to a pattern of chemically sensible bond distances for molybdenum(VI) phosphate materials. The bond valence sums for the refined model are significantly improved over those from the previous structural model. Each Mo(VI) octahedra is found to have two short, two medium, and two long bond lengths in the structure, a result obtained from the refinement of the model against the diffraction data and not enforced by soft restraints. The P−O−P bond angle within the structure was calculated to be 150.2(5)°, compared to 141.0° in the published structure.

The precise bond length distribution in γ-$(MoO_2)_2P_2O_7$ can be rationalized by the zigzag nature of the Mo octahedral chain, a short portion of which is shown in Figure 7. The shortest bond in each of the octahedra is to the terminal oxygen (O8 and O9). The bonds trans to O8 and O9, namely, Mo2−O7 and Mo1−O4, respectively, are "long" bonds; however, these two lengths differ significantly between the two octahedra, being 2.483 and 2.148 Å, respectively. These differences arise

(34) Wells, A. F. *Structural Inorganic Chemistry*, 5th ed.; Clarendon Press: Oxford, 1984.
(35) Ok, K. M.; Halasyamani, P. S.; Casanova, D.; Llunell, M.; Alemany, P.; Alvarez, S. *Chem. Mater.* **2006**, *18*, 3176–3183.
(36) Costentin, G.; Leclaire, A.; Borel, M. M.; Grandin, A.; Raveau, B. *Rev. Inorg. Chem.* **1993**, *13*, 77–101.

Table 1. Bond Lengths and Bond Valence Sum Values in γ-$(MoO_2)_2P_2O_7$, As Given in the Published Model,[12] and Those Calculated from the Model Refined Using a Combination of Synchrotron and Neutron Data in this Work[a]

		published model		combined model	
central atom	apex atom	bond length /Å	O BVS /vu	bond length /Å	O BVS /vu
Mo1	O9:1	1.835	1.126	1.6565(56)	1.825
	O7:1	1.950	1.263	1.6930(59)	1.849
	O2:0	1.858	2.041	1.9716(38)	2.102
	O2:1	1.858	2.041	1.9716(38)	2.102
	O4:1	1.898	1.848	2.1482(61)	1.989
	O6:0	2.080	1.568	2.2717(55)	1.949
	BVS /vu	5.60		5.86	
Mo2	O8:0	1.842	1.105	1.6737(66)	1.742
	O6:0	1.884	1.568	1.7043(55)	1.949
	O1:1	1.957	1.834	1.9603(38)	2.119
	O1:0	1.957	1.834	1.9603(38)	2.119
	O3:1	2.107	1.703	2.0689(68)	1.901
	O7:0	2.185	1.263	2.4827(59)	1.849
	BVS /vu	4.69		5.74	
P1	O4:0	1.605	1.848	1.4524(69)	2.119
	O1:4	1.588	1.854	1.5022(42)	2.119
	O1:5	1.588	1.854	1.5022(42)	1.989
	O5:1	1.644	2.011	1.5466(77)	2.209
	BVS /vu	3.98		5.31	
P2	O2:4	1.610	2.041	1.5004(41)	1.901
	O2:5	1.610	2.041	1.5004(41)	2.209
	O3:0	1.548	1.703	1.5061(42)	2.102
	O5:0	1.599	2.011	1.5892(77)	2.102
	BVS /vu	4.15		4.99	

[a] BVSs were calculated using R_{ij}[Mo(VI)] = 1.8790 Å,[37] R_{ij}[P(V)] = 1.604 Å and b = 0.37 Å.[38]

as the former bond is part of the Mo−O−Mo backbone, whereas the latter bond forms an Mo−O−P linkage. This can be rationalized in terms of the BVSs of the O atoms: if the P1−O4 bond in the Mo1−O4−P1 linkage is ∼1.5 Å, the BVS contribution to O4 is 1.32, leading to an ideal Mo−O bond length of 2.02 Å (valence = 0.68). For an Mo−O bond of ∼2.5 Å, the BVS contribution from the Mo−O bond would be only 0.19, leading to an underbonded O.

Along the Mo−O−Mo chain the presence of a long Mo−O bond length (e.g., Mo2−O7) causes the next O−Mo bond length (Mo1−O7) to be shorter to maintain the bond valence on the O atom. The remaining two bonds on each of the octahedra (not pictured) are medium length (Mo1−O2 and Mo2−O1), leading to the overall pattern of two short, two medium, and two long bonds.

Low Temperature Structure of α-$(MoO_2)_2P_2O_7$. Variable temperature X-ray powder data in Figure 3 clearly showed the existence of weak superstructure peaks at low temperatures. Electron diffraction was used to investigate the formation of a superstructure and showed that commensurate satellite reflections were present at G ± m/4[2,-1,0]*, Figure 8. These satellite peaks could be indexed to a supercell using the transformation matrix (1 2 0, −1 2 0, 0 0 1) with lattice parameters a∼17.83 Å, b∼17.83 Å, and c∼10.38 Å, α∼β∼γ∼90°. The characteristic extinction condition ($F(hk0)$ = 0 unless h is even) is apparent in the zero-order Laue zone (ZOLZ) region (Figure 7a) of ⟨001⟩ zone axis electron diffraction patterns (EDPs). This requires the presence of an a-glide perpendicular to c.

Considering group-subgroup relationships for a displacive phase transition using this transformation matrix, it was not possible to obtain tetragonal symmetry (as might be implied by the cell metric) or to retain orthorhombic symmetry. Reduction of the lattice symmetry to monoclinic or triclinic must occur, though it is clear from the EDPs that β is ∼90°. Possible isotropy subgroups are $P2_1/c$, Pc, $P2_1$, $P\bar{1}$, and $P1$. Of these $P2_1/c$ and Pc (in the standard settings corresponding to a ∼ 17.83 Å, b ∼ 10.38 Å, and c ∼ 17.83 Å, β ∼ 90.2°) are consistent with observations from electron diffraction. An SHG test showed no frequency doubling. Although not definitive, this is consistent with the centrosymmetric space group $P2_1/c$.

A starting model was generated for the superstructure using knowledge of the high temperature subcell model and the cell transformation matrix using ISODISPLACE.[39] The model contained 8 Mo atoms, 8 P atoms, and 44 O atoms in the asymmetric unit. None of these atoms were on special positions. Refinements of the low temperature superstructure were carried out using simultaneous fitting of the synchrotron X-ray and TOF neutron data both recorded at 250 K. The data sets were weighted to ensure they both contributed approximately equally to the refinement. Bond lengths had soft restraints applied during simulated annealing. P−O bonds were restrained to be 1.507 and 1.580 Å (P−O(−Mo) and P−O(−P) respectively), Mo−O bond restraints were as follows: short 1.65 Å, medium 1.99 Å, and long

(37) Zocchi, F. *Solid State Sci.* **2000**, *2*, 383–387.
(38) Brese, N. E.; O'Keeffe, M. *Acta Crystallogr., Sect. B* **1991**, *47*, 192–197.
(39) Campbell, B. J.; Stokes, H. T.; Tanner, D. E.; Hatch, D. M. *J. Appl. Crystallogr.* **2006**, *39*, 607–614.

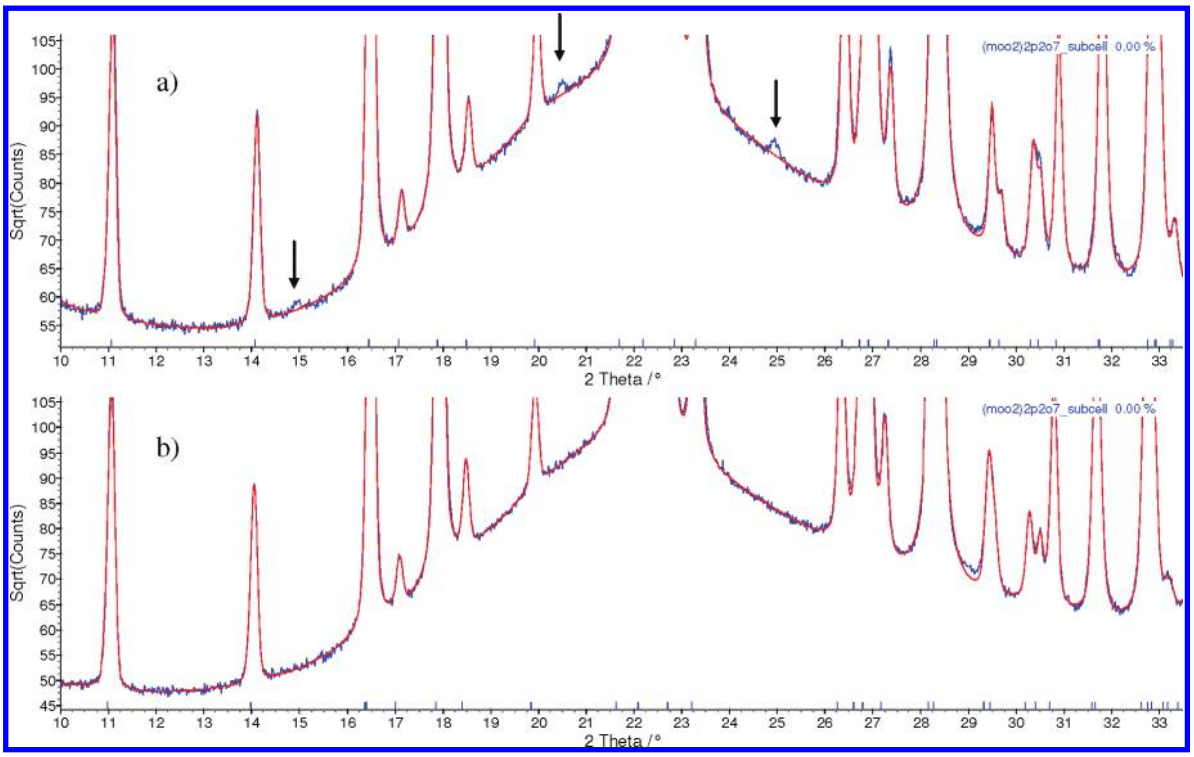

Figure 3. Pawley fits of X-ray diffraction data of $(MoO_2)_2P_2O_7$ using the *Pnma* subcell on data recorded at (a) 303 K and (b) 423 K. Weak peaks at 2θ = 14.80, 20.40, and 24.93° are visible at 303 K, disappear above 377 K, and reappear on cooling. The figure shows the experimental data in blue and the Pawley fits in red. Data are shown on a $\sqrt{\ }$ I scale to emphasize weak features. The strongest reflection has a peak height of ~300,000 counts.

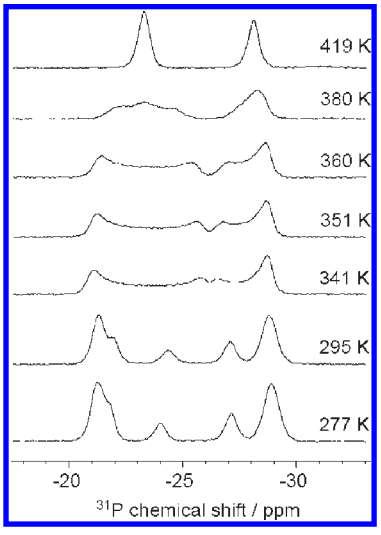

Figure 4. Center band regions of ^{31}P MAS NMR spectra of $(MoO_2)_2P_2O_7$ as a function of temperature, recorded at a spinning speed of 5 kHz.

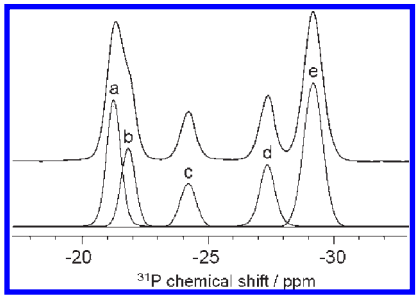

Figure 5. Deconvolution of the 1D ^{31}P NMR spectrum of $(MoO_2)_2P_2O_7$ recorded at 277 K.

2.15/2.35 Å. The bond angles were restrained to be 90 and 180° in the octahedra and 109.47° in the tetrahedra; all restraints had sufficient weighting to retain sensible polyhedral geometry of the structure. Several thousand cycles of randomization and convergence were applied to the coordinates within the model. The best solution gave excellent agreement to the diffraction data with an overall R_{wp} of 3.85%. The Rietveld fits are given in Figure 9; selected refinement details are given in Table 3.

Fractional coordinates are given in CIF format in the Supporting Information. Histograms of derived bond distributions are plotted in the Supporting Information Figure S3; average bond lengths are given in the Supporting Information Table S3 for each bond type. As observed in the high temperature structure, the distribution of bond lengths is as expected for the 48 Mo−O bonds in the low temperature structure: 8 short bonds (1.65 Å), 8 slightly longer bonds (~1.7 Å), 20 medium bonds (2 Å), 8 medium long bonds (2.15 Å), and 4 very long bonds (2.4 Å). The P−O bonds can be separated into P−O(−Mo) and P−O(−P) bonds, having distributions with a mean of 1.51 and 1.57 Å respectively; however, the distributions have spreads that cause them to overlap. Bond valence sums for all Mo and P sites deviate by <0.22 units from average values. Minimum, maximum, and average values for Mo(VI) are 5.74−6.11, average = 5.83 units; minimum, maximum, and average values for P(V) are 4.80−5.03, average = 4.96 units.[38] P−O−P bond angles are given in Table 4; we note that in the low-temperature superstructure we obtain angles 142.8(4)°, 157.4(5)°, 139.3(4)°, and 140.5(4)° compared

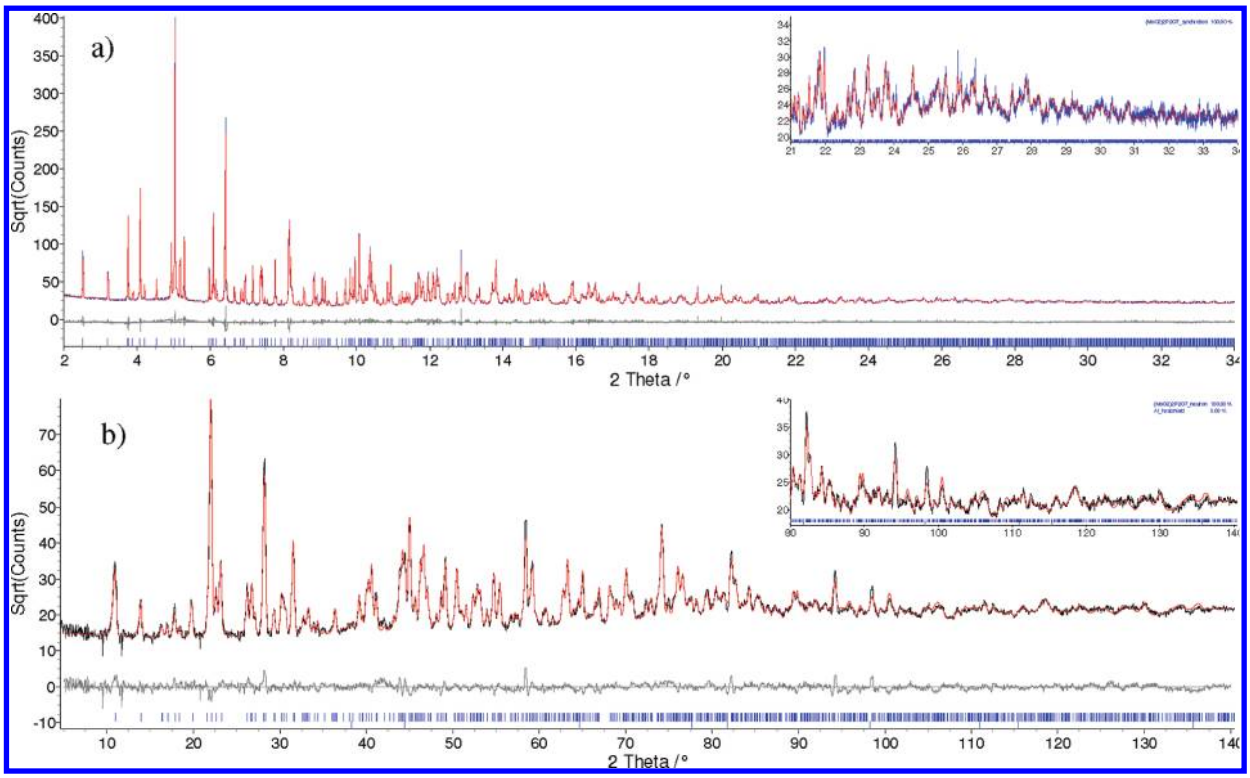

Figure 6. Rietveld fit of the high temperature powder data shown on a $\sqrt{I}$ scale to emphasize the weak features in the data. (a) Synchrotron data recorded at 423 K. Inset: 2θ range 21−34°. The R_{wp} for this fit was 7.91%. (b) Neutron data recorded at 500 K. Inset: 2θ range 80−140°. The R_{wp} for this fit was 7.45%. Experimental data in blue/black, calculated pattern in red, and difference plot in gray.

Table 2. Selected Crystallographic Data and Refinement Details from the High Temperature Combined X-ray and Neutron Refinement in Space Group *Pnma*[a]

a /Å	12.6577(1)	overall R_{wp} /%	7.78
b /Å	6.3095(1)	X-ray R_{wp} /%	7.91
c /Å	10.4161(1)	neutron R_{wp} /%	7.45
volume /Å^3	831.87(2)	X-ray R_{Bragg} /%	3.93
number of parameters	104	neutron R_{Bragg} /%	4.53
space group	*Pnma*	GOF	2.80

[a] Quoted cell parameters are the values refined against the X-ray data (423 K).

to 150.2(5)° at high temperature. In the high temperature structure the torsion angle in the P_2O_7 group is fixed at 0° by symmetry; torsion angles in the low temperature structure vary from 0.7−3.5°, that is, the P_2O_7 groups remain essentially eclipsed.

While an excellent fit has been obtained using a combined X-ray/neutron analysis with data from two of the world's highest resolution diffractometers, the fact that 180 structural parameters have been refined means that supporting data from other techniques to corroborate the model is crucial. The ^{31}P NMR spectrum of this phase, Figure 5 shows five resolved resonances, with an intensity ratio of 2:1:1:1:3. This is consistent with the presence of four crystallographically independent P_2O_7 groups, with three groups in similar environments giving rise to signals a, b, and e, and the fourth group in a distinctly different environment (signals c and d). This distinction is confirmed by the $^2J_{PP}$ coupling constants obtained from spin echo experiments, shown in Table 5 and in the Supporting Information Figures S4 and S5. The extracted *J* couplings for sites a, b, and e are very similar, and distinct from the average value of 29.5 ± 0.2 Hz obtained from signals c and d. This is consistent with signals c and d arising from one P_2O_7 group with three other P_2O_7 groups giving rise to signals a+b and e.

Spin echo experiments were also performed to obtain $^2J_{PP}$ coupling constants for the signals in the spectrum of the high temperature phase. These are identical within the fitting error, confirming that the signals arise from inequivalent P sites with the same (unique) P_2O_7 environment.

The $^2J_{PP}$ coupling constant is expected to be strongly correlated with the P−O−P bond angle in the pyrophosphate unit, and should thus provide useful insight into the local structure. Gaussian calculations were performed on isolated $P_2O_7^{4-}$ groups to investigate this correlation. Figure 10 shows a monotonic increase in $^2J_{PP}$ with increasing P−O−P angle in both staggered and eclipsed geometries. The NMR results thus agree well with results of the Rietveld refinement, Table 4, which shows that the P−O−P bond angles fall into two groups: a set of three P_2O_7 groups with angles between 139−143° (J ~11 Hz), and a P_2O_7 group with a distinct larger bond angle around 157° (J ~30 Hz). We can therefore assign signals c and d to the P11−O52−P22 group of the superstructure.

Significant additional information can be obtained using 2D NMR experiments. Figure 11 shows a *J*-based (through-bond) DQ/SQ correlation experiment at different temperatures which confirm the linkages proposed from the measurements of the *J* coupling constants. The cross-peak connecting P1 and P2 in the high temperature phase confirms they are part of the same P_2O_7 unit. The weak diagonal peaks in this spectrum are not true correlation peaks. Their intensity decreases with increasing spinning rate, showing that they are due to "rotational resonance" effects[20] and can be ignored.

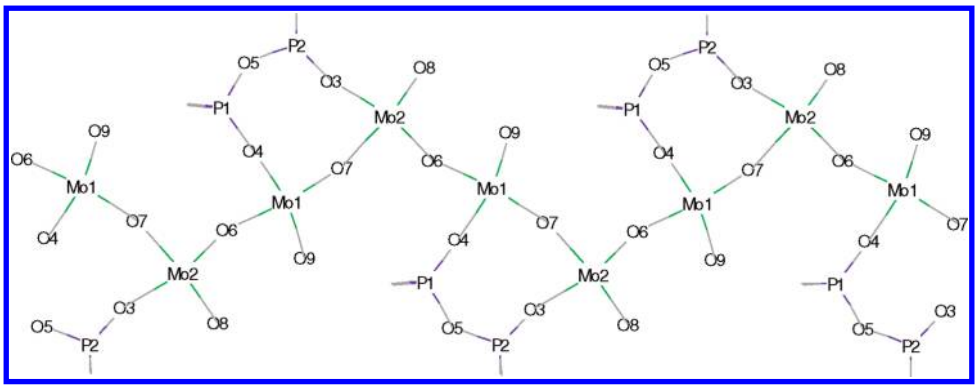

Figure 7. Section of the MoO_6 chain structure in γ-$(MoO_2)_2P_2O_7$ in the *ac* plane; each octahedron contains additional O's above and below the plane.

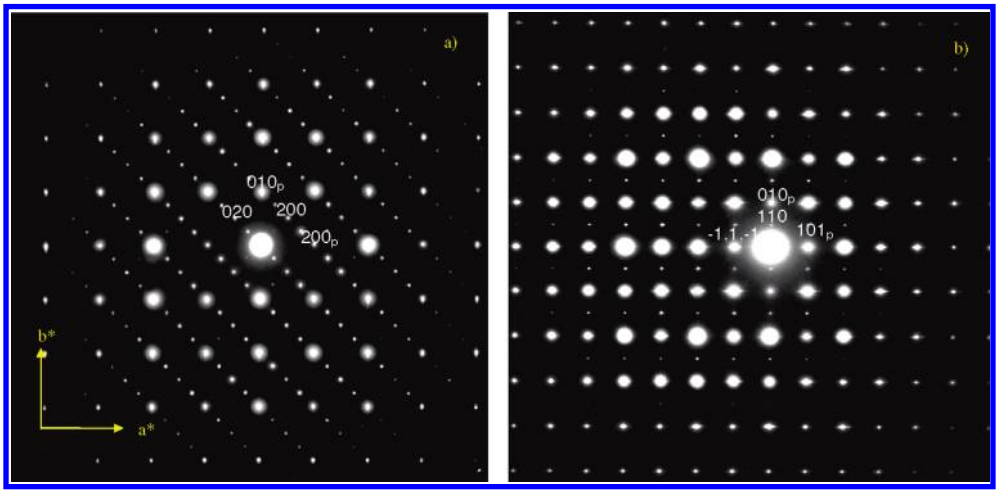

Figure 8. Electron diffraction patterns of α-$(MoO_2)_2P_2O_7$ with zone axes (a) [001] and (b) [1,−1,2], indexed with respect to both the *Pnma* parent substructure (labeled with the subscript p) and the supercell structure. Note the characteristic extinction condition $F(hk0) = 0$ unless $h = 2n$ in (a), requiring the presence of an *a*-glide perpendicular to *c*. Axes labels are with respect to the parent substructure.

The low temperature spectrum, Figure 11c confirms the previously established correlation between peaks a+b and e on the one hand, and c and d on the other. The spectrum of the intermediate β phase is particularly significant as it shows a smooth pattern of correlation between P1 and P2 type sites across the width of the spectrum. Spin echo experiments on this phase (not shown) also confirm that the *J* coupling varies smoothly between 10−21 Hz as a function of chemical shift, suggesting that there is an effectively continuous distribution of P−O−P angles over a somewhat smaller range than that observed in the α-phase.

Another significant feature of the correlation experiments is the distinct shape of the correlation peaks, which are angled along the spectrum diagonal. This indicates that each peak is associated with a distribution of NMR frequencies. The spin−echo experiments, which refocus such "inhomogenous" distributions, show that the underlying "homogeneous" line width, $1/\pi T_2'$, is of the order of 8 Hz, while the peaks have overall linewidths much larger than this, of at least 120 Hz. Calculation of the magnetic susceptibility tensor for the high symmetry phase using CASTEP gives an estimate for the anisotropy of the susceptibility, $\Delta\chi = -0.058$ ppm, which corresponds to a line broadening of $|4\pi\Delta\chi| = 0.73$ ppm or ∼150 Hz at the ^{31}P NMR frequency.[24] Hence the 2D line shape and the resolution in the 1D spectrum is essentially determined by the anisotropy of susceptibility rather than other factors, such as a static distribution of chemical environments.

The dipolar-based (through space) DQ/SQ correlation experiments probe interatomic distances,[40] *r*, since the dipolar coupling is proportional to r^{-3}. The shortest inter-P distances are those within individual P_2O_7 groups, which are typically between 2.9 and 3.2 Å, and so are associated with the strongest dipolar couplings values. Figure 12 shows selected P_2O_7 groups in α-$(MoO_2)_2P_2O_7$, which shows that the next largest P,P couplings are those between P1*n* and P2*n* sites, where P1*n* and P2*n* denote sites derived from P1 and P2 respectively in the high temperature structure. A given P site will couple to multiple nearby P sites, and so it is not sufficient to consider simply the shortest interatomic distances. To a first approximation, however, the overall rate of build of a correlation peak between site *i* and a set of spins of type *J* is determined by the root-sum-square coupling.[41]

$$d_{\mathrm{rss}}(i,J) = \sqrt{\sum_{j\in J} d_{ij}^2}$$

(40) Harris, R. K. *Nuclear magnetic resonance spectroscopy: a physicochemical view*; Pitman: London, 1983.
(41) Zorin, V. E.; Brown, S. P.; Hodgkinson, P. *Mol. Phys.* **2006**, *104*, 293–304.

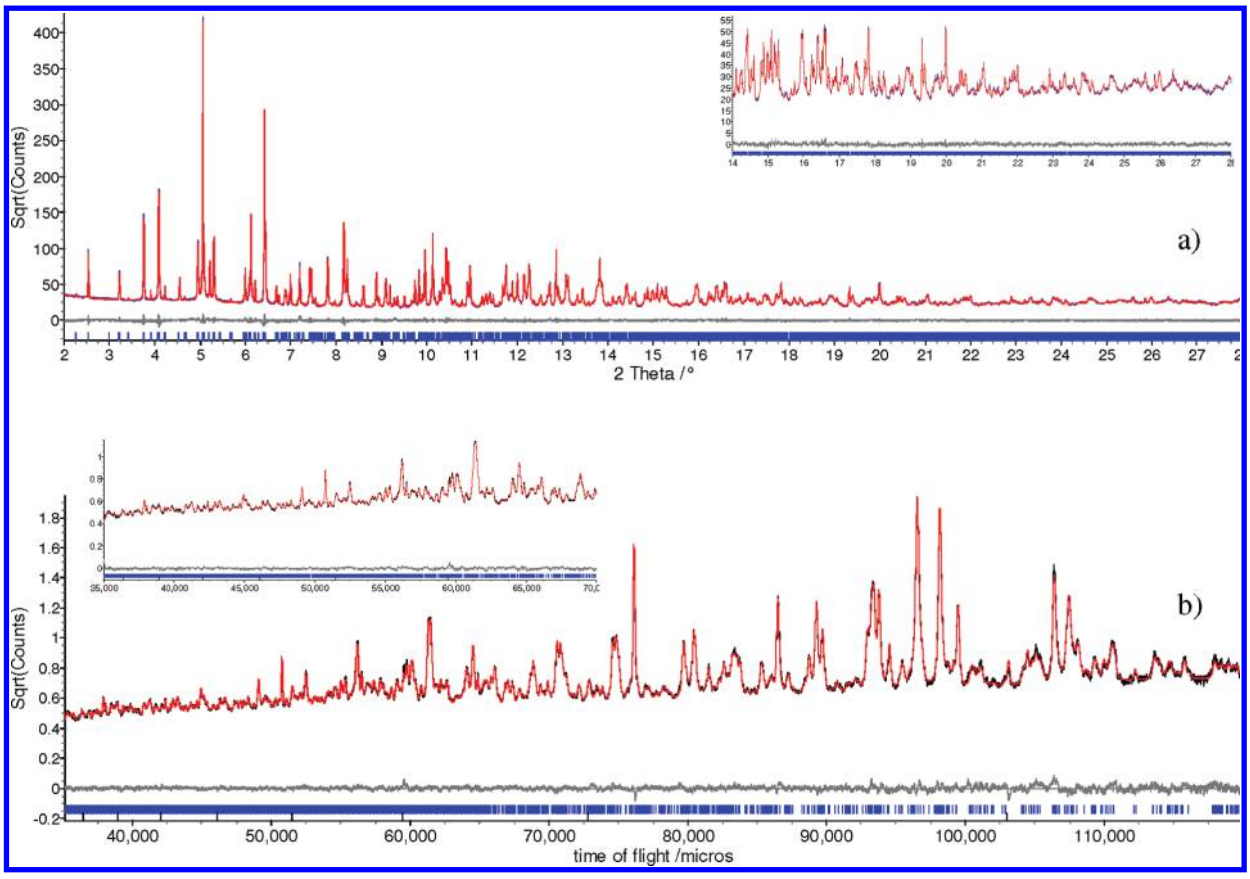

Figure 9. Fit of the low temperature model to the data recorded at 250 K. (a) Synchrotron data. Inset: 2θ range 14−28°. The R_{wp} for this fit was 5.22%. (b) Neutron TOF data, d = 0.62−2.49 Å. Inset: The TOF range 35−70 ms, d = 0.62−1.45 Å. The R_{wp} for this fit was 2.97%. The figure shows the experimental data in blue/black, the calculated pattern in red, and the difference plot in gray. Data plotted on a $\sqrt{I}$ scale to emphasize the weak features in the data.

Table 3. Selected Crystallographic Data and Refinement Details from the Low Temperature Combined X-ray and Neutron Refinement in Space Group $P2_1/c$ (T = 250 K)

a /Å	17.8161(3)	overall R_{wp} /%	3.85
b /Å	10.3672(1)	X-ray R_{wp} /%	5.22
c /Å	17.8089(3)	neutron R_{wp} /%	2.97
β /deg	90.2009(2)	X-ray R_{Bragg} /%	1.84
volume /Å^3	3289.34(7)	neutron R_{Bragg} /%	1.79
number of parameters	239	GOF	1.55

Table 4. P−O−P Bond Angles in the $P2_1/c$ Superstructure

P−O−P angle	bond angle /deg
P14−O51−P21	142.8(4)
P11−O52−P22	157.4(5)
P12−O53−*P*23	139.3(4)
P13−O54−P24	140.5(4)

where d_{ij} is the dipolar coupling between spins i and j. To include the effect of longer range P−P interactions, a 5 × 5 × 5 supercell was generated from the unit cell of the low temperature structure. The root-sum-square couplings were then calculated for the distinct P environments in the central unit cell. Table 6 confirms that dipolar couplings are strongest within a P_2O_7 group (~670 Hz and above) and otherwise the P1*n* sites mostly couple to P2*n* sites with effective couplings of ~300 Hz.

Figure 13 shows dipolar-based DQ/SQ correlation experiments acquired at two different dipolar mixing times. At short mixing times (a), two strong correlations, between peaks a/b and e, and peaks c and d, are observed

Table 5. $^2J_{PP}$ Coupling Constants and T_2' Values from Fitting Spin-Echo Experiments at 260 and 433 K on α- and γ-$(MoO_2)_2P_2O_7$[a]

		line a	line b	line c	line d	line e
250 K	T_2'/ms	38	42	43	45	33
	J/Hz	10.3	9.1	29.2	29.8	11.8
423 K	T_2'/ms	18	19			
	J/Hz	14.6	14.6			

[a] The (random) fitting error on the J values is about ±0.2 Hz.

because of strong intra-P_2O_7 phosphorus dipolar coupling. These correspond to the correlation peaks observed in the J-based experiment, Figure 11c.

At a longer mixing time, Figure 13b, new peaks appear which correspond to inter P_2O_7 group couplings, which can be used to help assign the spectrum. We start with the assumption that resonance c is due to P11 and d is due to P22 (the spin−echo experiments show they are P11 and P22, and we justify the assignment of P11 vs P22 below). The autocorrelation peaks a/b, a/b, and e,e arise from a combination of multiple longer range dipolar couplings and are not particularly informative. The d_{rss} values reported in Table 6 suggest that the first inter-P_2O_7 correlation peaks for P11 (resonance c) should arise with a P2*n* type (P23 or P24) phosphorus, while P22 (resonance d) is expected to be correlated with P12 and P13. This suggests that the overlapped resonances a+b are due to P21/P23/P24 sites, while peak e is likely to correspond to the unresolved P12/P13/P14 sites.

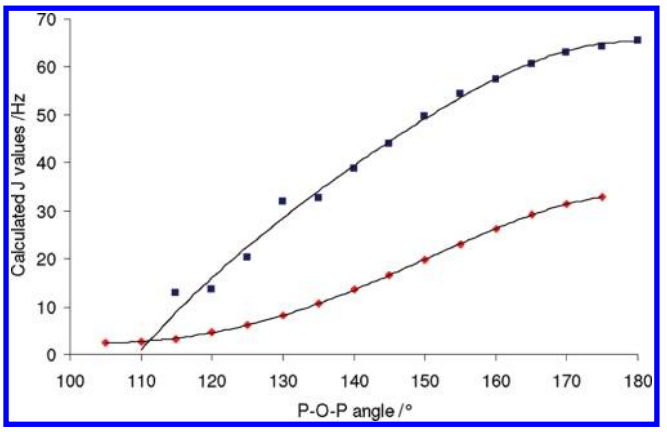

Figure 10. Evolution of the calculated *J* coupling constant as a function of the P−O−P bond angle in an eclipsed (blue solid squares) and a staggered (red solid diamonds) configuration of the $P_2O_7^{4-}$ unit.

Moreover, no correlation is observed between resonances c and e (even at longer mixing times) suggesting that all the P1*n* (except P11) resonances contribute to e. Similarly the lack of a correlation between a/b and e confirms that all the P2*n* (except P22) contribute to the a+b signal. The key insight from the dipolar-based experiments is that the P11 and P22 sites are changed significantly by the structural distortions and "cross sides" of the spectrum.

The assignment of peak c as P11 as opposed to P22 is inferred from CASTEP calculations on the high and low temperature structures. In both cases P1*n* sites are calculated to be more strongly shielded than the P2*n* sites, and have a chemical shift more negative by ~6 ppm (in good agreement with the data of Figure 4). The calculations have to be treated with some caution given the complexity of the structure and the inherent limitations of DFT calculations, estimated as ± 2 ppm for the first row elements, but they confirm that distortions in P_2O_7 groups of the magnitude observed are sufficient to influence the ^{31}P spectrum in the manner observed. Spectra were also simulated for simple models with the P−O−P constrained to different angles between 130 and 170° and the rest of the structure optimized using DLS methods (Supporting Information Figure S6).[42] These show a significant, approximately linear reduction in chemical shift difference of 10.5 to 4.4 ppm over this angular range.

Intermediate Structure of *β*-$(MoO_2)_2P_2O_7$. The presence of a new phase intermediate between the high (γ) and low temperature (α) structures is hinted at by the unusual evolution of cell parameters in Figure 2 between 325 and 377 K and a second discontinuity at 377 K. The electron diffraction patterns in Figure 8 were all recorded at ambient temperature and showed a commensurate superstructure. A small number of images, such as that in Figure 14, showed the presence of incommensurate satellite reflections. It is possible that beam heating was sufficient to drive these crystallites through the 325 K phase transition. The extra satellite peaks are present along the parent *a** direction.

At intermediate temperatures, there are also marked changes in the 1D NMR data of Figure 4, with the evolution of significant intensity in the region between the high temperature resonances. This is consistent both with the formation of an incommensurate phase and the suggestion that the P11 and P22 sites "cross". No further investigation has been undertaken in this temperature region.

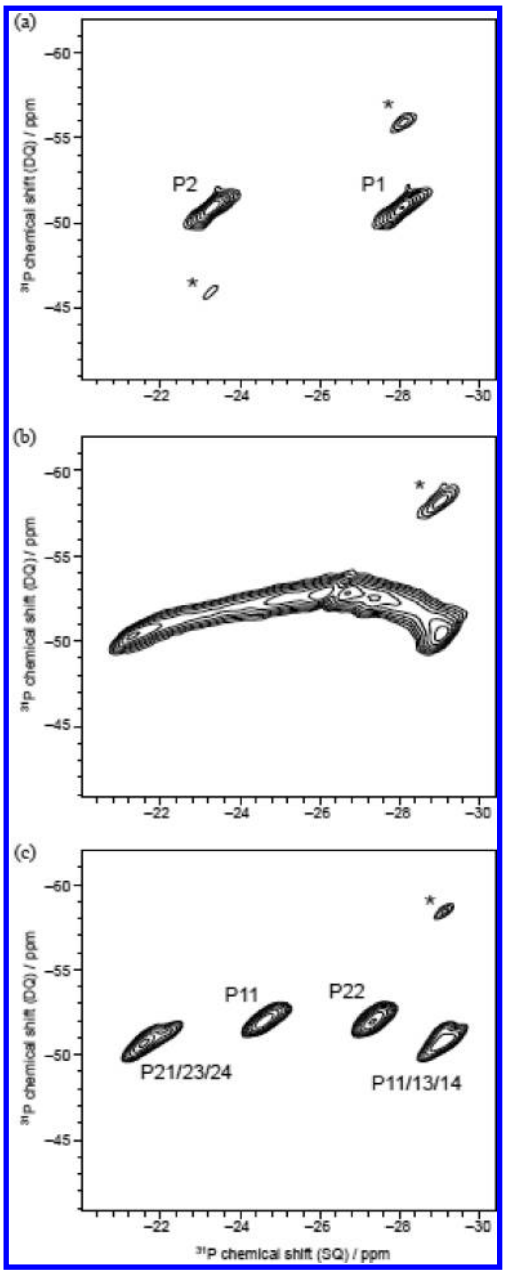

Figure 11. *J*-based DQ/SQ correlation refocused (INADEQUATE) spectra of $(MoO_2)_2P_2O_7$ recorded at sample temperatures of (a) 431 K, (b) 331 K, and (c) 297 K. Pairs of peaks with the same double quantum frequency across the diagonal reveal coupling interactions between the sites. The peaks along the spectrum diagonal marked with an asterisk are due to rotational resonance effects and can be ignored.

Discussion

The experiments described above reveal a fascinating series of structural transitions in $(MoO_2)_2P_2O_7$ which can only be fully understood by combination of a range of experimental probes, each with different intrinsic sensitivity to the structural changes that occur. Powder diffraction reveals the presence of phase transitions via both the peak intensities

(42) Meier, W. M.; Villiger, H. *Z. Kristallogr. Kristallgeom. Kristallphys. Kristallchem.* **1969**, *129*, 411–423.

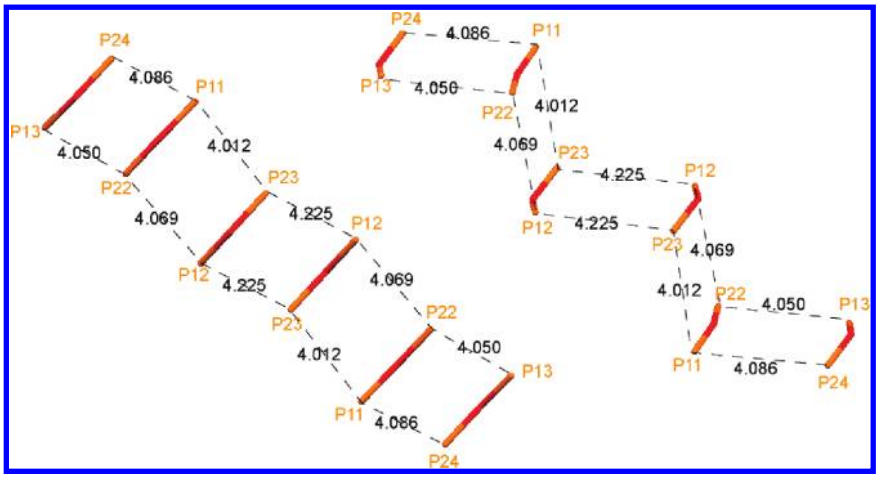

Figure 12. Spatial arrangement of P1−O5−P2 related fragments in α-$(MoO_2)_2P_2O_7$. The chain is shown in two different orientations.

Table 6. Effective (Root-Sum-Square) $^{31}P,^{31}P$ Dipolar Couplings (in Hertz) between the Eight P Sites in the Low Temperature $P2_1/c$ Model Structure[a]

	P11	P12	P13	P14	P21	P22	P23	P24
P11	66							
P12	188	184						
P13	190	146	66					
P14	146	64	184	184				
P21	190	71	**296**	**777**	159			
P22	**674**	**348**	**313**	108	122	80		
P23	**317**	**825**	184	72	78	203	170	
P24	**305**	111	**772**	**336**	203	173	126	78

[a] The highlighted boxes indicate the dipolar coupling values calculated for pairs of sites belonging to the same P_2O_7 group. Bold values refer to other stronger couplings referenced in the text.

and their positions. The additional peaks due to the low temperature superstructure, are, however, relatively weak in both X-ray (Figure 3) and neutron data sets, such that the most useful information comes from the thermal expansion data of Figure 2. Here the high resolution, high q synchrotron data and resulting high precision cell parameter determination is particularly important in identifying two discontinuities in the temperature dependence of the cell volume and identifying phase boundaries. In contrast to diffraction methods, the local probe of ^{31}P NMR provides striking and direct evidence for significant structural changes between 325 and 377 K.

Above 377 K two peaks are present in the 1D spectra, which arise from the two P atoms present in a single crystallographically unique P_2O_7 group, as later confirmed by 2D through bond and J coupling experiments. This suggests that the high temperature structure can be adequately described using a *Pnma* subcell model similar to that originally proposed by Kierkegaard.[12] Refinement of this model against X-ray and neutron powder diffraction data led to a structure containing a sensible distribution of bond lengths and BVS values. The good fit to the diffraction data point to this being a high quality structural model.

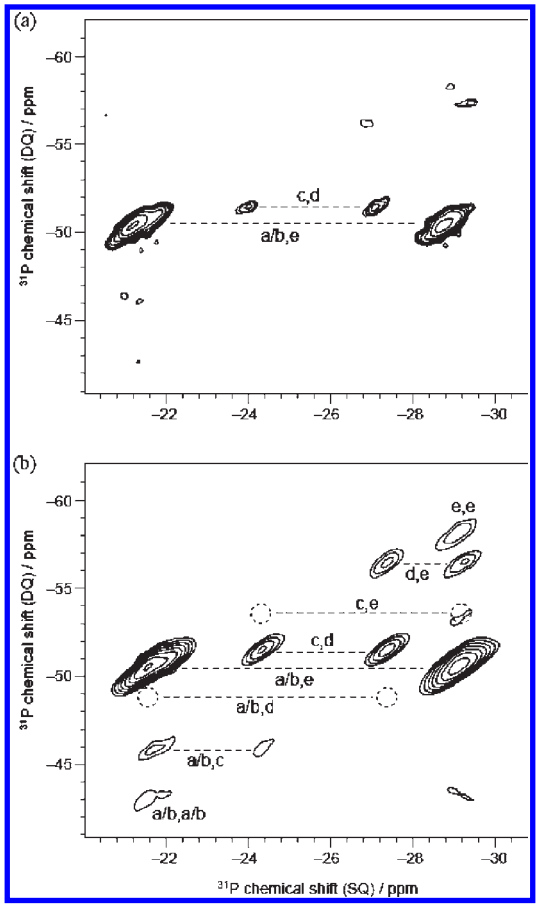

Figure 13. ^{31}P DQ/SQ correlation experiment with a dipolar mixing times of (a) 0.14 ms and (b) 0.36 ms, at an MAS rate of 8 kHz and a sample temperature of 283 K. The dotted circles indicate absent correlations discussed in the text.

Cooling below 377 K leads to significant changes in the 1D (Figure 4) and 2D (Figure 11) NMR data. The range of resonances observed and intensity build up in the region between the high temperature resonances is consistent with the structure becoming incommensurate in this temperature range. This is supported by electron diffraction data.

Below 325 K all experimental observations are consistent with a lock-in transition. The NMR pattern sharpens to 5 resolved resonances with a 2:1:1:1:3 intensity ratio. This is

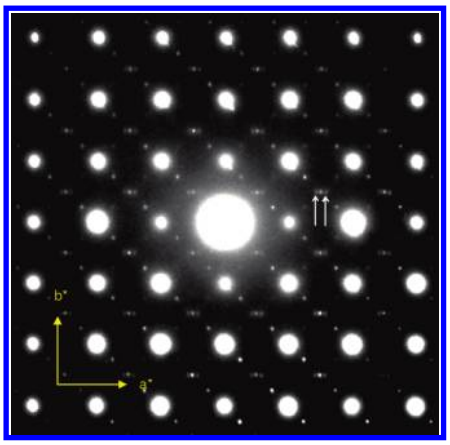

Figure 14. Electron diffraction patterns of β-$(MoO_2)_2P_2O_7$ with zone axis [001]. Incommensurate peaks are indicated by arrows.

consistent with four unique P_2O_7 groups, three of which are in similar environments. The low intensity of supercell reflections in the diffraction data suggests the transition is displacive in nature. The low temperature cell can be derived from electron diffraction data and the extinction symbol *P-c-*, the absence of an SHG signal, the symmetry requirements imposed by the displacive nature of the transition and the NMR data are all consistent with the space group symmetry $P2_1/c$. The structure can then be solved using simulated annealing from the ideal high temperature coordinates, leading to a model in excellent agreement with the powder diffraction data and having a sensible distribution of bond lengths and angles within coordination polyhedra.

It is interesting to consider the driving force for the complex superstructure at room temperature. As with related materials it is presumably caused by a balance of local bonding requirements within coordination polyhedra and achieving optimal intrapolyhedral angles constrained by the topology of the strongly bonded framework. Focusing on P−O−P linkages, the high temperature structure has a single angle of 150.2(5)° while the low temperature structure has four unique P_2O_7 groups with bond angles 142.8(4)°, 157.4(5)°, 139.3(4)°, and 140.5(4)°. The low temperature average is 145°, around 5° lower than at high temperature, reflecting the volume-reducing nature of the transition. This average is close to the expected value of ∼145° from calculations on staggered P_2O_7 groups[43] and 142° (α-$Mo_2P_4O_{15}$)[10] and 145.6° (ZrP_2O_7)[9] observed experimentally in other well characterized pyrophosphate supercell systems. The diffraction data suggest that with this topology one P−O−P linkage is forced to have a significantly larger bridging angle than the other three. Despite the complexity of the structure and the fact it was derived from powder data, the bond angle distribution is entirely consistent with the 1D NMR in terms of peak intensities (peaks c and d of Figure 5 are $\sim^1/_3$ intensity of a+b and e) and *J* values (peaks c and d ∼30 Hz; a, b, and e ∼11 Hz).

Given the complexity of the low temperature structure and the high sensitivity of ^{31}P NMR shifts to small local structural distortions it is currently difficult to make fully quantitative use of the low temperature NMR data. Nevertheless CASTEP calculations show that small local distortions of the P_2O_7 groups as revealed by powder diffraction data lead to significant changes in chemical shifts. This is sufficient to cause "peak crossing" such that P1*n* and P2*n* resonances can reverse in order. This is consistent with observations from 2D through-space NMR experiments which allow us to suggest a tentative assignment of the 1D patterns. The "peak crossing" leads to a build up in intensity in the chemical shift range between the two high temperature resonances as P_2O_7 units change geometry. The NMR data in the intermediate temperature range, where we believe the material to be incommensurate, are therefore consistent with the presence of a static range of P−O−P angles, as would be expected for a modulated structure.

Acknowledgment. We thank the EPSRC for funding under EP/C538927/1, STFC for access to ISIS and ESRF facilities, and the U.S. Commerce Department for access to the NCNR at NIST. S.E.L. thanks Durham University for a Doctoral Training Fellowship. We thank Irene Margiolaki at the ESRF, Sarah Poulton, and Mark Green at NIST, and Richard Ibberson at HRPD for assistance with data collections, P. Shiv Halasyamani for SHG measurements and Mark Fox for Gaussian calculations.

Supporting Information Available: Full description of the diffraction experiments and Rietveld refinements. X-ray crystallographic files in CIF format for the α- and γ- $(MoO_2)_2P_2O_7$ structures at 250 and 423 K respectively. Details of the 1D NMR fitting at high and low temperature. Tables and histograms showing the bond length distribution of the α-$(MoO_2)_2P_2O_7$ structure. Figures showing the evolution of the spin−echo decay for both the α- and γ- $(MoO_2)_2P_2O_7$ structures. Calculated spectra of the DLS-derived model structures with varying P−O−P bond angles. Complete reference 30. This material is available free of charge via the Internet at http://pubs.acs.org.

(43) O'Keeffe, M.; Domenges, B.; Gibbs, G. V. *J. Phys. Chem.* **1985**, *89*, 2304–2309.